ARTICLES
https://doi.org/10.1038/s41565-018-0318-5
nature nanotechnology

A DNA nanomachine chemically resolves lysosomes in live cells

KaHo Leung[1,2,3], Kasturi Chakraborty[1,2,3], Anand Saminathan[1,2] and Yamuna Krishnan[1,2*]

Lysosomes are multifunctional, subcellular organelles with roles in plasma membrane repair, autophagy, pathogen degradation and nutrient sensing. Dysfunctional lysosomes underlie Alzheimer's disease, Parkinson's disease and rare lysosomal storage diseases, but their contributions to these pathophysiologies are unclear. Live imaging has revealed lysosome subpopulations with different physical characteristics including dynamics, morphology or cellular localization. Here, we chemically resolve lysosome subpopulations using a DNA-based combination reporter that quantitatively images pH and chloride simultaneously in the same lysosome while retaining single-lysosome information in live cells. We call this technology two-ion measurement or 2-IM. 2-IM of lysosomes in primary skin fibroblasts derived from healthy individuals shows two main lysosome populations, one of which is absent in primary cells derived from patients with Niemann–Pick disease. When patient cells are treated with relevant therapeutics, the second population re-emerges. Chemically resolving lysosomes by 2-IM could enable decoding the mechanistic underpinnings of lysosomal diseases, monitoring disease progression or evaluating therapeutic efficacy.

Lysosomes are highly fusogenic organelles that regulate cellular processes such as innate immunity by fusion with the phagosome, cell membrane repair through fusion with the plasma membrane, autophagy by fusion with the autophagosome and nutrient sensing through the mTOR pathway[1]. Lysosome dysfunction is central to the pathology of common neurological disorders such as Alzheimer's disease, Parkinson's disease as well as ~60 rare, largely untreatable genetic diseases called lysosomal storage diseases[2]. It has been challenging to deconvolute how each of the multiple roles of lysosomes is affected in the diverse pathophysiologies associated with lysosome-related diseases.

Lysosomes are, by and large, regarded as a single population while assaying for a specific lysosomal function. However, recent promising studies have considered that subpopulations of lysosomes might perform subsets of tasks[3]. Indeed, many cell types have evolved specialized lysosomes that perform distinct functions. For instance, in addition to lysosomes, skin cells have melanosomes[4], neutrophils have azurophil granules[5], cytotoxic T-cells have secretory lysosomes[6] while every cell has autolysosomes[7]. Functional imaging based on physical parameters such as lysosome movement, morphology or spatial position within cells has revealed subpopulations that exhibit different behaviours and functions[3,8]. For example, autolysosomes and lysosomes adopt tubulovesicular and vesicular morphologies, respectively[9]. Lysosomes have also been sorted into two populations based on how actively they move within the cell[10]. Spatial positioning of lysosomes is emerging as a correlate of lysosome function[11,12] which is mediated by the cytoskeleton, the endoplasmic reticulum (ER) and lysosomal biogenesis[13]. Nevertheless, the capacity to chemically discriminate between lysosome populations in live cells would significantly aid our understanding of lysosome biology by providing the ability to quantitatively correlate chemotypes with function. For example, in the 1960s, electron microscopy and bright-field imaging could only distinguish up to three stages in melanosome maturation based on morphology and melanin content, respectively[14]. However, when protein markers were used to chemotype melanosomes, it revealed four stages in melanosome maturation. Chemical resolution revealed the colourless, stage I melanosome that had eluded identification until then due to its high physical and morphological similarity with lysosomes[15]. However, there are still no methods to chemically resolve lysosome populations.

Specialized lysosomes have a different protein composition from normal lysosomes to enable the distinct biochemistries within their lumens. This lumenal biochemistry is facilitated by an optimal chemical milieu, of which key components are high concentrations of specific ions homeostatically maintained by the lysosome protein composition[16,17]. H^+ and Cl^- are two highly abundant ions in the lysosome that are critical to its function[18]. In fact, no other organelle has a greater concentration of either ion. Lysosomal pH is critical to lysosome maturation, cargo degradation and recycling of degraded material[19]. High lumenal Cl^- in the lysosome is required for the activity of certain lysosome-resident hydrolases[16,20]. However, unlike other organelles, lumenal Cl^- levels in the lysosome are independent of lumenal pH[16,21]. We therefore hypothesized that the levels of H^+ and Cl^- in the lysosome could form a basis to chemically discriminate lysosome populations in live cells.

Here, we show that by measuring two ions—H^+ and Cl^-—simultaneously in the same lysosome and retaining this information with single-lysosome addressability, one can resolve lysosomal subpopulations quantitatively in live cells. We call this technology two-ion measurement or 2-IM. A technology such as 2-IM has proved elusive to realize thus far for several reasons. Cl^--sensitive small-molecule probes offer the necessary chemical selectivity, molar brightness and long-wavelength excitation, but not the required spatial addressability or organelle targetability[22]. Genetically encoded Cl^- sensors offer stable spatial localization, but the response of these reporters to Cl^- is pH sensitive[23]. This complicates analysis of most organelles as lumenal Cl^- entry is coupled to their acidification. Fluorescent proteins label organelles with lower specificity than endocytic tracers and have lower dynamic range compared with DNA-based nanodevices[23,24]. DNA nanodevices comprise a range of biologically interfacable[25], quantitative imaging probes that unite

[1]Department of Chemistry, The University of Chicago, Chicago, IL, USA. [2]Grossman Institute of Neuroscience, Quantitative Biology and Human Behavior, The University of Chicago, Chicago, IL, USA. [3]These authors contributed equally: KaHo Leung, Kasturi Chakraborty. *e-mail: yamuna@uchicago.edu

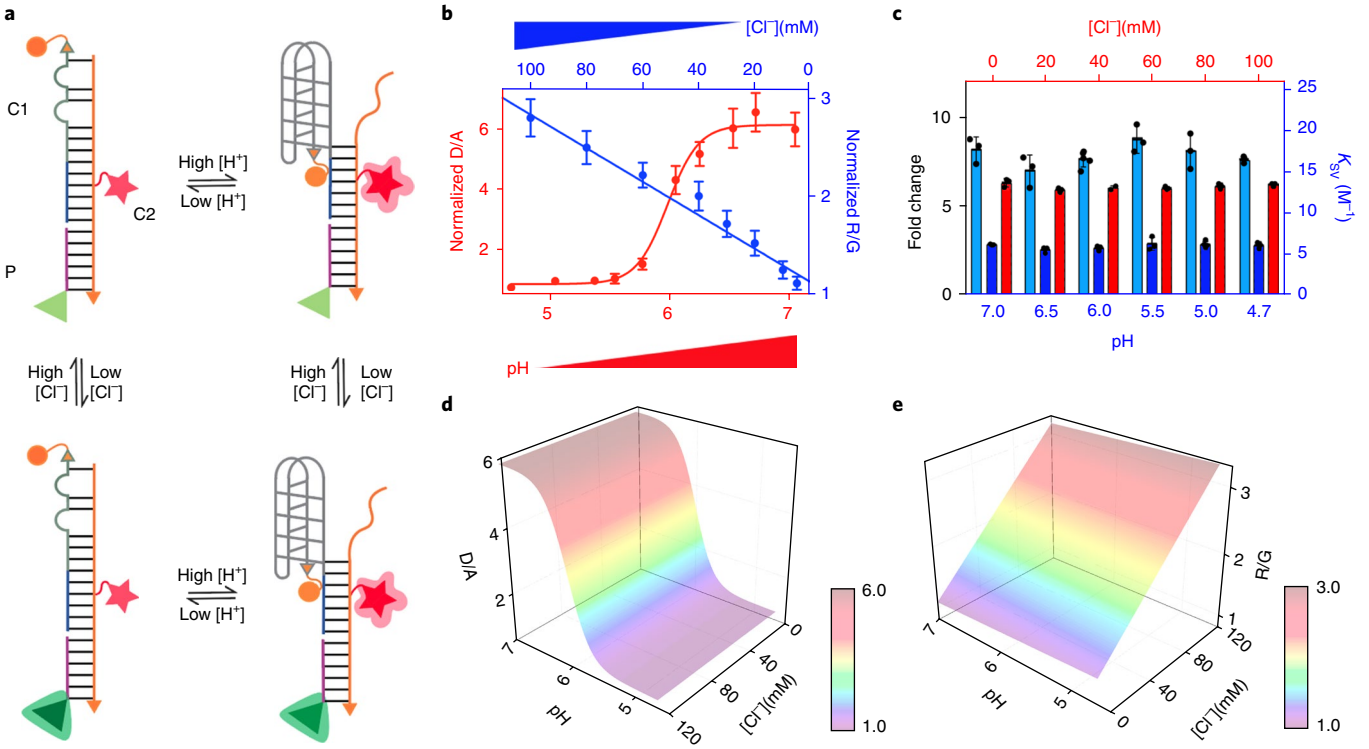

Fig. 1 | Design and characterization of ChloropHore. a, Schematic of the working principle. A pH-induced change in fluorescence resonance energy transfer between Alexa 546 (donor, orange sphere) and Alexa 647 (acceptor, red star) reports pH ratiometrically. A Cl^--sensitive fluorophore (BAC, green triangle) and Alexa 647 reports Cl^- ratiometrically. P, Cl^--sensing module (purple line) containing a Cl^--sensitive fluorophore BAC; C1, pH-sensing module containing i-motif sequence (grey line); C2, normalizing module (orange line) containing a pH, Cl^--insensitive fluorophore Alexa 647. **b**, pH and Cl^- response profiles of ChloropHore. Normalized fluorescence intensity ratio (D/A) of donor (D) and acceptor (A) on donor excitation in vitro as a function of pH and 50 mM Cl^- (red). Normalized fluorescence intensity ratio (R/G) of Alexa 647 (R) and BAC (G) as a function of Cl^- concentration at pH 7 (blue). Values were normalized to R/G at 5 mM Cl^- or D/A at pH 4. **c**, Performance of the pH-sensing module (red) at different [Cl^-] and of the Cl^--sensing module at different pH values (blue). Fold changes in D/A (red bars) or R/G (dark blue bars) for the pH- and Cl^--sensing modules are shown. Stern–Volmer constant (K_{SV}, light blue bars) for Cl^- sensing at each pH is also shown. **d**,**e**, Calibration surface plots of D/A (**d**) and R/G (**e**) of ChloropHore as a function of Cl^- and pH. Error bars indicate the mean ± standard error of the mean (s.e.m.) of three independent measurements.

the photophysical advantages of small molecules, the stable localization provided by proteins along with the precision of organelle targeting that is accessible to endocytic tracers[17,26–29].

By using a DNA nanodevice that can ratiometrically image pH and [Cl^-] simultaneously with single-lysosome addressability, we could discriminate lysosome chemotypes on a 2D map that correlates lumenal pH with lumenal [Cl^-]. Lysosome profiles of cells obtained from healthy individuals revealed a high-chloride, high-acidity population that was absent in cells derived from patients afflicted with Niemann–Pick A, B or C diseases. Interestingly, treating these cultured patient cells with the known therapeutic for these diseases led to a re-emergence of the high-chloride, high-acidity population.

Design and in vitro characterization of ChloropHore

We describe the design, creation and characterization of a DNA-based, ratiometric, fluorescent combination reporter of pH and chloride called ChloropHore. ChloropHore is a 61-base pair DNA duplex comprising three strands C1, C2 and P (Supplementary Table 1) and bears three distinct domains (Fig. 1a). Two of these are fluorescent, ratiometric reporter domains that have previously reported, namely a Cl^- reporter domain, *Clensor*[17,30] and a pH reporter domain called the *I-switch*[16,26,31–33]. Each reporter domain is fused to either end of an 'integration domain', which comprises a 27-mer duplex, that serves to integrate the pH and the Cl^- reporter domains into a single DNA assembly. This 27-mer duplex also helps in targeting, because its anionic nature aids recognition and trafficking by scavenger receptors in a DNA-sequence-independent manner. To match the pH sensing regime of ChloropHore to the low pH regimes encountered in mammalian lysosomes we also made $ChloropHore_{Ly}$, a variant that used modified 5′-bromocytosines in the C-rich region (Supplementary Table 1)[31,34]. The formation and specificity of ChloropHore and $ChloropHore_{Ly}$ were confirmed by a gel shift assay, circular dichroism spectroscopy and UV melting studies (Supplementary Figs. 1–3).

The fluorescence response characteristics of ChloropHore and $ChloropHore_{Ly}$ were investigated as a function of pH and [Cl^-] in order to determine their pH and [Cl^-] sensitive regimes. The gradual increase of the donor (D) to acceptor (A) fluorescence intensity ratio (D/A) of ChloropHore and $ChloropHore_{Ly}$ revealed their pH reporting capabilities between pH 5.5 and 6.5 (Fig. 1b) and pH 4.5 and 6.5, respectively (Supplementary Fig. 4b), the latter being well suited to measure the pH of highly acidic human lysosomes. Both ChloropHore and $ChloropHore_{Ly}$ show a sigmoidal increase in D/A as a function of pH in the sensitive regime, and fold changes in D/A of 5.5 and 3, respectively. Notably, the fold change in the D/A ratio remained invariant for both ChloropHore and $ChloropHore_{Ly}$ over [Cl^-] ranging from 5 mM to 120 mM (Fig. 1c and Supplementary Fig. 4c). Thus, the pH-sensing characteristics of ChloropHore and $ChloropHore_{Ly}$ are insensitive to changes in physiological [Cl^-]. This is illustrated by a 3D surface plot of D/A as a function of pH performed at different fixed values of [Cl^-], as shown in Fig. 1d (Supplementary Fig. 4d).

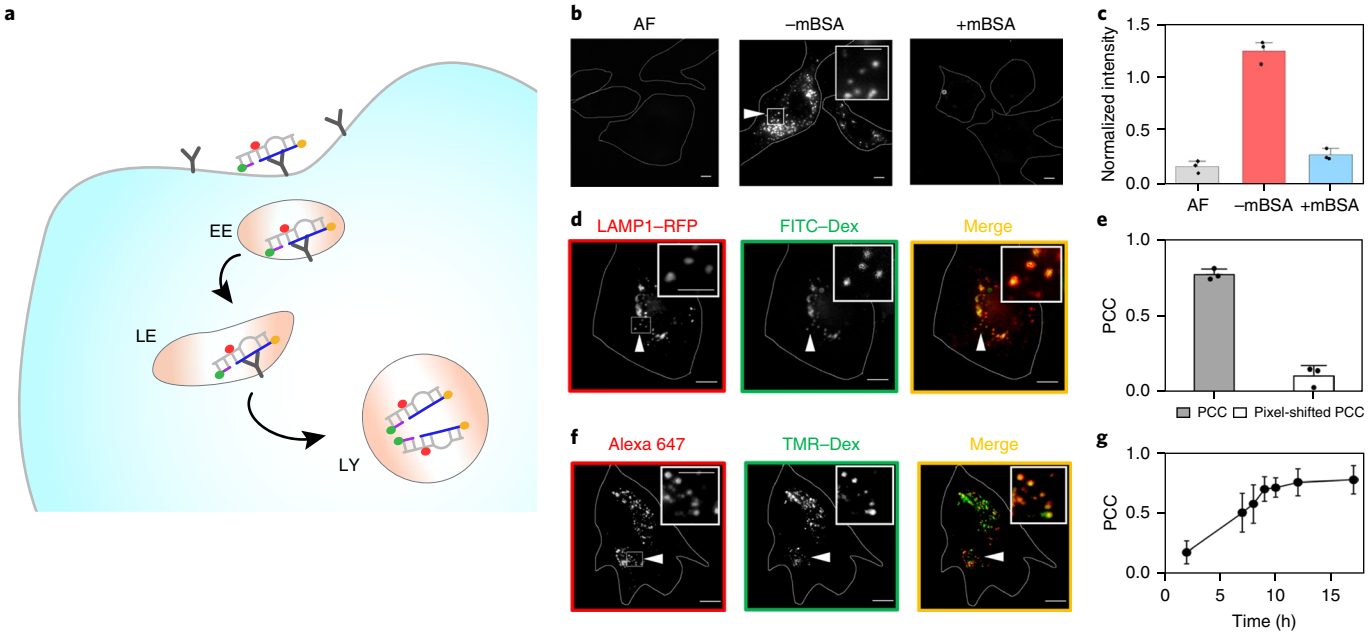

Fig. 2 | Trafficking pathway of ChloropHore in human dermal fibroblasts. a, Trafficking of ChloropHore along the scavenger receptor-mediated endocytic pathway (EE, early endosome; LE, late endosome; LY, lysosome). **b,c**, ChloropHore uptake in primary skin fibroblasts (HDF cells) is competed out by excess maleylated BSA (mBSA, 10 μM). Cells are imaged in the Alexa 647 channel. AF, autofluorescence. **d**–**g**, ChloropHore labels lysosomes in HDF cells. **d**, Representative images of colocalization between lysosomes of HDF cells labelled with FITC–Dextran (green) and LAMP1–RFP (red) with the corresponding Pearson's correlation coefficient (PCC, **e**). **f**, Representative images of lysosomes of HDF cells labelled with TMR–Dextran (green) and ChloropHore (Alexa 647, red). **g**, Pearson's correlation coefficient of colocalization between ChloropHore and lysosomes as a function of ChloropHore chase times. Scale bars, 10 μm; inset scale bars, 5 μm. Experiments were performed in triplicate. Error bars indicate the mean of three independent experiments ± s.e.m. ($n = 20$ cells).

In parallel, the Alexa 647 (R) to BAC (G) fluorescence intensity ratio (R/G) shows a linear dependence with increasing [Cl^-], showing ~2.5-fold change on increasing [Cl^-] from 5 mM to 120 mM (Fig. 1b,c and Supplementary Fig. 4b,c). Again, for both ChloropHore and ChloropHore$_{Ly}$, the Stern–Volmer constant (K_{sv}) and the fold change in R/G stayed constant as a function of pH from pH 4.5–7.0 (Fig. 1c and Supplementary Fig. 4c). This is illustrated by a 3D surface plot of R/G as a function of [Cl^-] performed at different fixed values of pH as shown in Fig. 1e (Supplementary Fig. 4e). Thus, the [Cl^-] sensing characteristics of ChloropHore and ChloropHore$_{Ly}$ are insensitive to changes in physiological pH. This indicates that in ChloropHore and ChloropHore$_{Ly}$, the sensing characteristics of the H^+-sensing module is unaffected by integration to the Cl^--sensing module and vice versa, thus enabling potential detection of these two ions in parallel.

Two-ion measurement with single-endosome addressability

To simultaneously measure lysosomal pH and [Cl^-] in live cells, we targeted ChloropHore to the lysosomes of human dermal fibroblasts (HDF). HDF express scavenger receptors (SR) that uptake anionic ligands[35]. Therefore, DNA nanodevices can be trafficked to organelles on the endolysosomal pathway in diverse living systems[25,33,36–38] (Fig. 2a). On incubating 1 μM of ChloropHore with HDF cells for 1 h (referred to as 1 h 'pulse'), we found excellent uptake into punctate endosomes. The uptake was effectively competed out by 10 equivalents of maleylated bovine serum albumin (mBSA), revealing that in HDF cells ChloropHore is internalized via the SR pathway[35] (Fig. 2b,c).

We then estimated the time required for lysosomal localization of ChloropHore, by its time-dependent colocalization with a lysosomal marker. Pulsing HDF cells with 10 kDa fluorescent dextrans (0.25 mg ml^{-1}) for 1 h followed by a 16 h chase effectively marked lysosomes, as revealed by colocalization with LAMP1 fused to red fluorescent protein (LAMP1–RFP) (Fig. 2d,e). Next, we pulsed ChloropHore in HDF cells where lysosomes were prelabelled with tetramethylrhodamine labelled dextran (TMR–Dextran) as above, washed and imaged the cells at various chase times. ChloropHore and TMR–Dextran showed maximal colocalization at 9 h (Fig. 2f,g and Supplementary Fig. 5). Stability measurements revealed that ChloropHore and ChloropHore$_{Ly}$ had a half-life of 20 h and were stable for at least 10 h in HDF lysosomes[39] (Supplementary Fig. 5).

Next, we investigated the in-cell pH- and [Cl^-]-sensing characteristics of ChloropHore. We clamped lumenal pH and [Cl^-] in ChloropHore-labelled HDF cells by incubation in clamping buffers of fixed pH and [Cl^-] containing nigericin, monensin and tributyltin chloride at high [K^+][16,17]. Figure 3a shows representative fluorescence images of a cell clamped at the indicated pH and [Cl^-] imaged in the D, A, R and G channels along with the corresponding D/A and R/G maps. Histograms of D/A and R/G values of 150 endosomes clamped at different pH and [Cl^-] are shown in Supplementary Fig. 6. ChloropHore showed approximately a 5.5-fold change in D/A value from pH 4.0 to pH 7.0 across all tested values of [Cl^-], with the in vitro 3D surface plot being quantitatively recapitulated in cells (Fig. 3b and Supplementary Fig. 7). Similarly, ChloropHore response in terms of R/G as a function of [Cl^-] was determined at different fixed values of physiological pH (Fig. 3c). Both the K_{sv} and fold change in R/G from 5 mM to 120 mM [Cl^-] was constant from pH 4.0–7.0, with the in vitro 3D surface plot of R/G being quantitatively recapitulated in cells (Fig. 3c and Supplementary Fig. 7). This revealed that ChloropHore and ChloropHore$_{Ly}$ can simultaneously report pH and [Cl^-] with performance characteristics in cells that closely match their in vitro pH- and [Cl^-]-sensing properties.

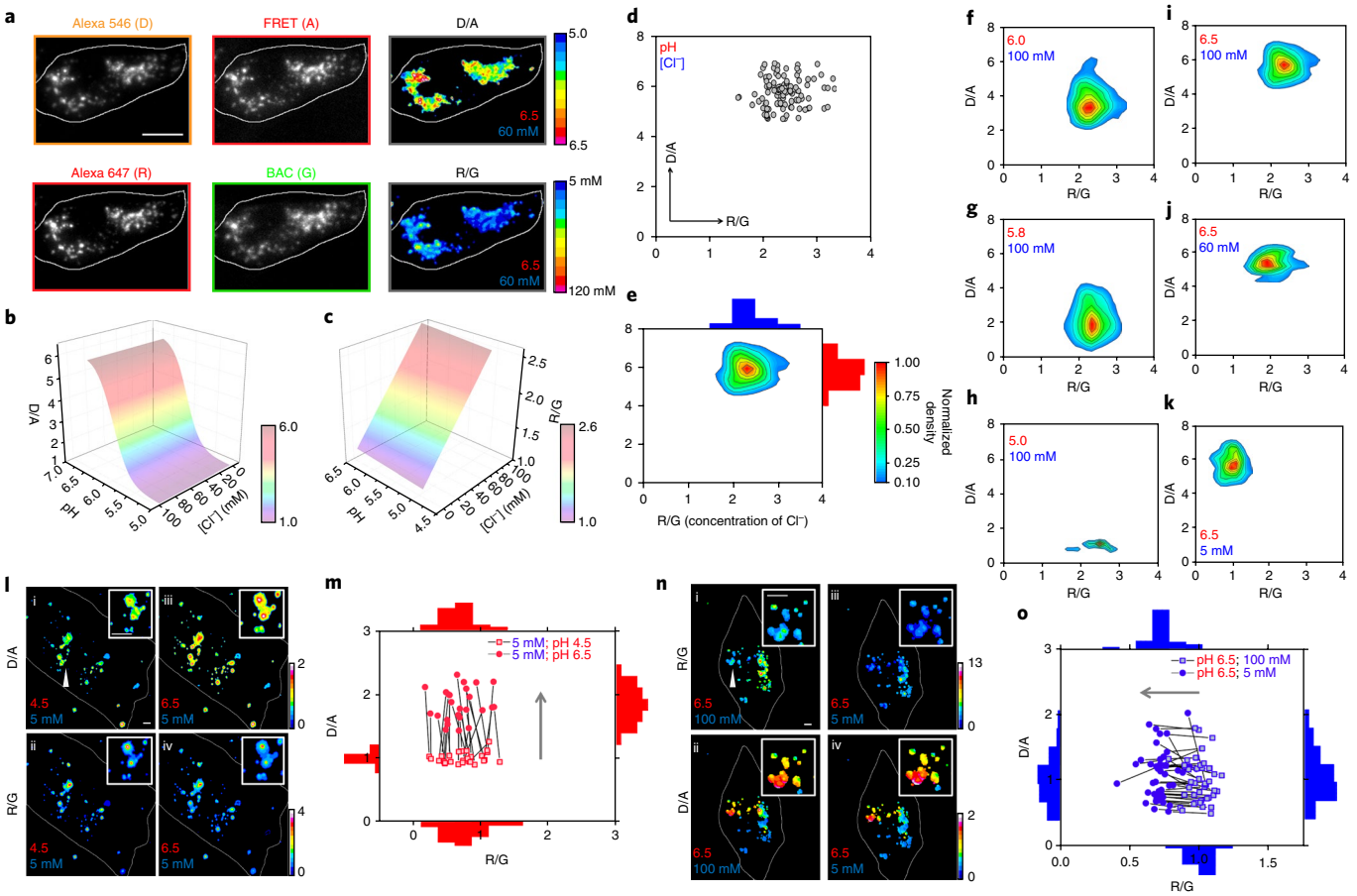

Fig. 3 | Intracellular calibration of ChloropHore and ChloropHore$_{Ly}$. **a**, Fluorescence images of primary HDF cells labelled with ChloropHore, clamped at the indicated pH and [Cl$^-$], imaged in the donor (D), acceptor (A), reference (R) and BAC (G) channels, and the corresponding pseudocolour D/A (pH) and R/G (Cl$^-$) maps. **b**,**c**, In-cell calibration surface corresponding to the pH and Cl$^-$ response profiles of the sensing modules in ChloropHore at various [Cl$^-$] and pH values, respectively. **d**, Representative scatter plot of D/A versus the R/G values of endosomes in primary HDF cells from a normal individual clamped at the indicated pH and [Cl$^-$]. Each data point corresponds to a single endosome. **e**, The scatter plot in **d** represented as a density plot and their projected histograms. The density plot was pseudocoloured, where red and blue correspond to populations with higher and lower frequencies of occurrence, that is, a 2-IM profile. **f**–**h**, 2-IM profiles of HDF cells clamped at indicated varying pH and fixed [Cl$^-$]. **i**–**k**, 2-IM profiles of HDF cells at fixed pH and varying [Cl$^-$]. For **a**–**k**, the experiments were performed in duplicate ($n = 15$ cells, $n = 150$ endosomes). **l**, Single-endosome clamping in HDF cells. ChloropHore-labelled cells clamped at indicated pH and [Cl$^-$] (i, ii) were clamped to a different pH and same [Cl$^-$] (iii, iv). **m**, 2D scatter plots and their projected histograms on a single axis of each clamping step of the same endosomes are shown. Grey arrow represents the direction of change in D/A (pH) values for each endosome. **n**, Chlorophore$_{Ly}$-labelled HDF cells clamped at indicated pH and [Cl$^-$] (i, ii) were clamped to the same pH but different [Cl$^-$] (iii, iv). **o**, 2D scatter plots and their projected histograms on a single axis for each clamping step. Grey arrow indicates direction of change in R/G (Cl$^-$) values for each endosome. Scale bars, 10 μm. For **l**–**o**, the experiments were performed in duplicate ($n = 30$ endosomes).

Next, we sought to simultaneously map both ions in endosomes while retaining this information with single-endosome addressability in live cells. Therefore, the D/A value (reflecting lumenal pH) in a given endosome is plotted against the R/G value (reflecting lumenal [Cl$^-$]) in the same endosome for 150 endosomes, which is represented as a scatter plot with each data point corresponding to a single endosome (Fig. 3d). For clearer visualization, these data are represented as a density plot colour-coded according to their frequencies of occurrence (Fig. 3e). We refer to this method of simultaneous quantitative imaging of two ions in a single endosome, while retaining concentration information with single-endosome addressability as 2-IM and the corresponding density plot as a 2-IM profile. Figures 3f–h show the 2-IM profiles of 150 endosomes clamped at the same [Cl$^-$] (100 mM) but different pH, while Figs. 3i–k show the 2-IM profiles of 150 endosomes clamped at the same pH (pH 6.5), but different [Cl$^-$].

To illustrate the capability of 2-IM to address single endosomes, we subjected ChloropHore$_{Ly}$-labelled HDF cells to different clamped states of pH and [Cl$^-$] in series due to ChloropHore$_{Ly}$'s optimal pH responsivity in lysosomes (Supplementary Fig. 8). ChloropHore$_{Ly}$-labelled endosomes were clamped at the indicated pH and [Cl$^-$] and imaged in D, A, R and G channels (Fig. 3l,n). Figure 3l(i,ii) shows the D/A and corresponding R/G maps of cells clamped at pH 4.5 and 5 mM Cl$^-$. The D/A and corresponding R/G maps of these same cells subsequently clamped at the same value of [Cl$^-$], but at pH 6.5 are shown in Fig. 3l(iii,iv) (Supplementary Fig. 9). Figure 3m shows a plot of individual endosomes in each clamped state, with black lines connecting the same endosome in either clamped state. It is clear that when [Cl$^-$] was constant and pH changed, all the endosomes showed increased D/A and negligible variation of R/G, moving parallel to the *y* axis. Similarly, Fig. 3n(i–iv) shows the D/A and R/G maps of cells clamped at 100 mM Cl$^-$ and pH 6.5 that have subsequently been clamped at the same value of pH, but at 5 mM Cl$^-$. Again, when pH was constant and [Cl$^-$] was changed, individual endosomes moved from right to left, parallel to the *x* axis (Fig. 3o). Thus, in addition to

population measurements, 2-IM provides information with single-endosome resolution.

2-IM chemically resolves lysosome populations

The 2-IM profile of lysosomes in fibroblasts of healthy individuals reveals populations with two distinct chemotypes. ChloropHore$_{Ly}$-labelled lysosomes in HDF cells were imaged to obtain D/A and R/G maps (Fig. 4a(i,ii)). The corresponding 2-IM profile revealed a major population of ~68% lysosomes that contained relatively low chloride, with R/G < 1.3 (Fig. 4b(i)). However, there is a minor population (~23%) with R/G > 1.5 and D/A < 1.25 with higher lumenal Cl^- and proton content (Fig. 4b(i)). This was consistent over experimental replicates on samples derived from the same individual as well as across multiple healthy individuals (Fig. 4b(i–vi)). 2-IM in lysosomes of diverse cell types such as BHK-21 cells, J774A.1 and T-47D cells also showed lysosome chemotypes with these characteristics (Supplementary Figs. 10–12). The high-chloride, high-acidity population was lost on pharmacologically inhibiting either V-ATPase or chloride channels with bafilomycin A1 or 5-nitro-2-(3-phenylpropylamino) benzoic acid, which selectively block lysosomal proton or Cl^- accumulation, respectively (Fig. 4c,d).

To see how these lysosomal populations are affected upon pathological lysosomal storage, we subjected fibroblasts of patients with lysosomal storage disorders to 2-IM profiling. Lysosomal storage disorders arise due to genetic defects in proteins that affect the lysosomal degradation of specific biomolecules. Further, dysfunctional lysosomes in a range of lysosomal storage disorders show reduced lumenal Cl^- and/or H^+ as a result of flawed lysosomal integrity[16]. We applied 2-IM to study three related lysosomal storage disorders, that is, the Niemann–Pick disease variants, due to their similarity of presentation, the fact that mutations lie in only one of three identified genes, all three gene products are lysosome-resident, and importantly, therapeutics are available for these diseases[40,41].

Niemann–Pick A (NP-A) and Niemann–Pick B (NP-B) diseases arise due to defects in the enzyme acid sphingomyelinase (ASM)[40], for which enzyme replacement therapy is available[42]. Niemann–Pick C (NP-C) disease arises due to defective cholesterol transport due to mutations in any one of two key proteins, NPC1 or NPC2 (ref. [41]), and for which clinical trials using cyclodextrin derivatives are under way[43]. Three patient samples corresponding to NP-A and NP-C disease and two for NP-B were studied based on sample availability, common mutations and characterization by enzyme activity (Supplementary Table 2).

After verifying that ChloropHore$_{Ly}$ could label the lysosomes in every patient sample (Supplementary Fig. 13), we subjected each sample to 2-IM (Fig. 4e). Typical D/A and R/G maps of ChloropHore$_{Ly}$-labelled lysosomes in fibroblasts derived from NP-A and NP-C patients are shown in Fig. 4a(iii–vi). The 2-IM profiles of fibroblasts derived from skin biopsies of all the patient samples showed that the high-chloride, high-acidity lysosome population was absent (Fig. 4e(i–viii)). Particularly, the 2-IM profile of NP-C patient samples showed a high degree of monodispersity compared with healthy samples (Fig. 4e).

Although lysosomal pH correlates with spatial position in certain cell types, no such dependence is available yet for lysosomal Cl^- (ref. [44]). Peripheral lysosomes show lower acidity in C2C12 murine myoblasts, human adipose microvascular endothelial cells and HeLa cells, but not primary human dendritic cells or Chinese hamster ovary cells[44]. Interestingly, 2-IM profiles in primary HDF cells showed that peripheral lysosomes had higher pH than perinuclear lysosomes (Fig. 4a(i), arrowhead). Further, in NP-A and NP-C cells the spatial heterogeneity in lysosomal pH is lost, with lysosomes becoming uniformly hypoacidic (Fig. 4a(iii,v)). In contrast to pH, no such spatial correlation could be observed for lumenal Cl^- in HDF cells from normal, healthy individuals (Fig. 4a(ii)). However, in NP-A and NP-C patient samples, the lumenal Cl^- of the perinuclear lysosomes was more affected and lower than those of peripheral lysosomes (Fig. 4a(iv,vi)). Taken together, this suggests that the milieu of the perinuclear lysosomes is more compromised than peripheral lysosomes, and that the high-chloride, high-acidity population could correspond to these lysosomes. We also explored whether there was any correlation between lumenal ions and lysosome size (Fig. 4f(i–iv)). These studies revealed that the high-chloride lysosomes were smaller in size in normal individuals, and their numbers were depleted in patient cells. No such clear correlation emerged for lysosomal pH.

ChloropHore$_{Ly}$ enables evaluation of therapeutic efficacy

To investigate how the high-chloride, high-acidity population was affected on inducing pathological lysosomal storage, we created cell culture models of NP-A/B and NP-C diseases. To mimic the sphingomyelin and cholesterol accumulation characterizing these disorders, we treated fibroblasts from a healthy individual with amitriptyline hydrochloride (AH)[45] and U18666A (ref. [46]) that inhibit ASM and NPC1, respectively. We performed 2-IM after verifying that ChloropHore$_{Ly}$ effectively labels lysosomes in these cells (Supplementary Fig. 13). The 2-IM profiles showed a monodisperse lysosome population in both cell culture models, and a depletion of the high-chloride, high-acidity lysosome population (Fig. 4g(i,ii)).

Next, we investigated whether this high-chloride, high-acidity lysosome population could be recovered on complementing patient cells with the corresponding therapeutic. Recombinant human ASM is used to treat NP-A/B patients by enzyme replacement therapy[42]. We therefore incubated fibroblasts from NP-A and NP-B patients with ASM as outlined in the literature[47]. These cells are expected to internalize ASM from the extracellular milieu, and traffic it to lysosomes, where it degrades sphingomyelin and mitigates storage[47]. The 2-IM profile of patient cells treated with ASM showed the reemergence of the high-chloride, high-acidity lysosome population (Fig. 4h(i,ii)).

Niemann–Pick C disease does not arise from the deficiency of a degradative enzyme, but rather due to a transport defect, for which there is still no therapeutic approved by the Food and Drug Administration. However, *o*-2-hydroxypropyl-β-cyclodextrin (βCD) treatment for 24 h has been shown to improve cholesterol transport from the lysosome to the endoplasmic reticulum, thereby delivering cholesterol to the endoplasmic reticulum for esterification and reducing storage in the lysosome[48]. Interestingly, treating NP-C patient samples mutated either in NPC1 (Fig. 4h(iii,iv)) or NPC2 (Fig. 4h(v)) with βCD showed a loss of monodispersity in the 2-IM profile and the appearance of lysosomes with higher lumenal Cl^- and H^+ content.

Conclusion

In summary, we have described a new technology to chemically resolve lysosome subpopulations in living cells based on the rationale that different subpopulations of lysosomes contain different ionic microenvironments that facilitate their distinct roles. This is a 2D method where quantification of two different ions in the lysosome, that is, lumenal pH and Cl^-, can be correlated with single-lysosome addressability. We exploit the principle that populations that are challenging to discriminate based on a single parameter, can be resolved in two dimensions based on a second independent parameter. This is seen in the case of 2D nuclear magnetic resonance spectroscopy and 2D gel electrophoresis[49]. However, to achieve this for organelles such as the lysosome, it is essential to be able to measure both parameters, that is, pH and Cl^- in parallel in a given lysosome, while retaining single-lysosome addressability.

The present combination reporter succeeds because it uses the 1:1 stoichiometry of DNA hybridization to integrate four functions with stoichiometric precision onto a single probe: (1) a pH-sensing

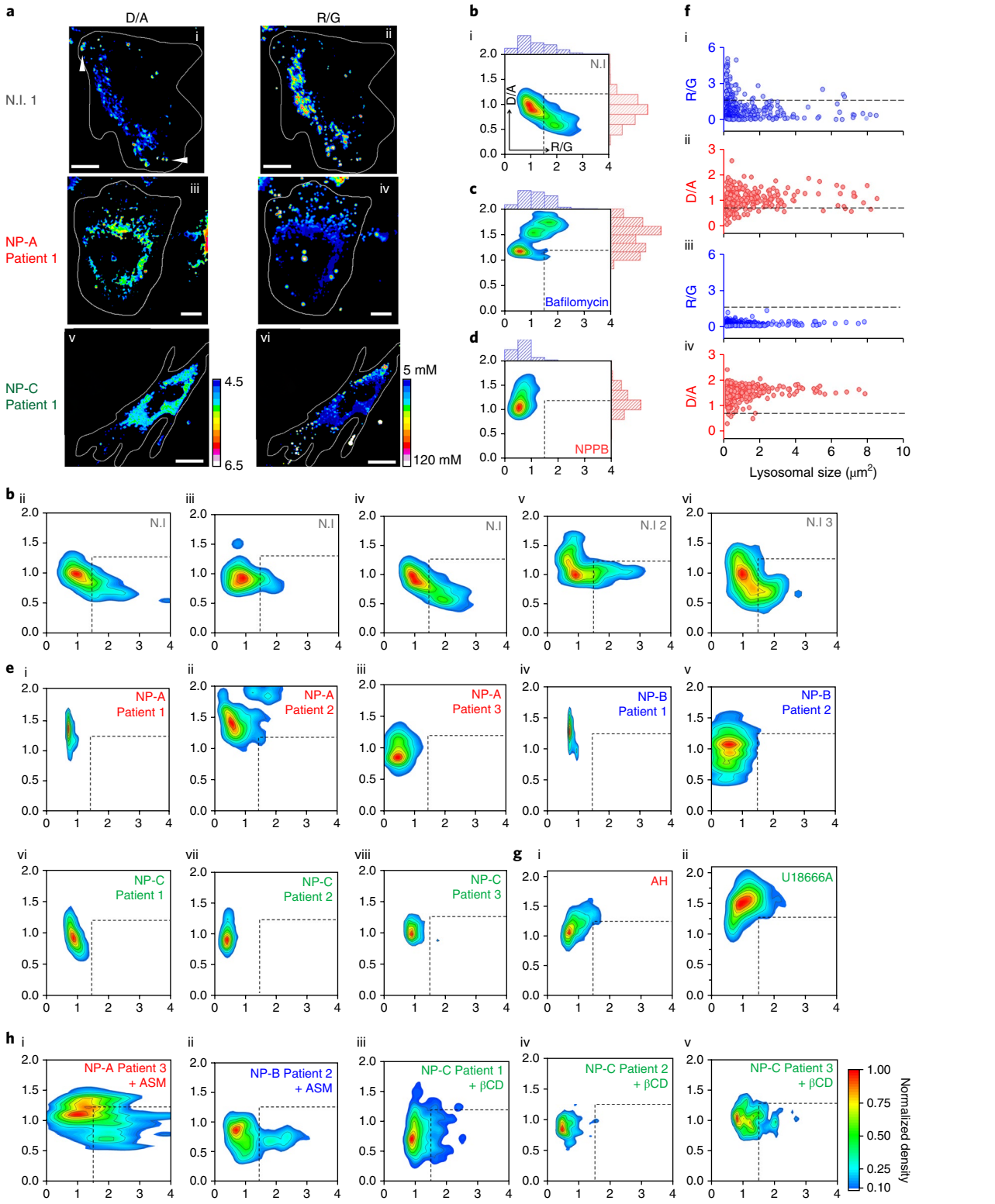

Fig. 4 | 2-IM chemically resolves lysosome populations. a, Respective pseudocolour D/A and R/G maps of HDF cells derived from normal, healthy individuals 1 (N.I. 1), NP-A patient 1 and NP-C patient 1 labelled with Chlorophore$_{Ly}$. **b**–**d**, 2-IM profiles and the corresponding histograms of D/A, R/G of normal individual (**b**(i)) and in the presence of 500 nM bafilomycin A1 (**c**) or 300 μM NPPB (**d**). **b**, 2-IM profiles of lysosomes of primary HDF cells from the same normal individual showing three replicates (ii–iv) and two different normal individuals 2–3 (v,vi). **e**, 2-IM profiles of lysosomes of primary skin fibroblasts derived from NP-A, NP-B and NP-C patients. **f**, Scatter plots of lysosome sizes versus their R/G or D/A values in a normal individual (i,ii) and an NP-A patient (iii,iv). **g**, 2-IM profiles of HDF cells treated with 65 μM amitriptyline (AH) or 20 μM U18666A. **h**, 2-IM profiles of NP-A and NP-B patient fibroblasts in the presence of 5 μg ASM and of NP-C patient fibroblasts in the presence of 50 μM βCD. Experiments were performed in duplicate ($n = 550$ lysosomes, $n = 55$ cells). Scale bars, 10 μm.

function; (2) a Cl^--sensing function; (3) an internal standard for simultaneous ratiometric quantitation of both Cl^- and pH; and (4) a lysosome-targeting function for addressability. 2-IM is a highly sensitive method that chemically resolved a high-chloride, high-acidity lysosome population in human fibroblasts isolated from skin biopsies of healthy humans. The significance of this high-chloride, high-acidity population was revealed upon 2-IM investigation of fibroblasts derived from skin biopsies of patients afflicted with three variants of Niemann–Pick disease, where this population was lost, resulting in highly monodisperse 2-IM profiles. Treating cells with the relevant therapeutic, that is, the defective enzyme, recovered the high-chloride, high-acidity population. However, treatment with a molecule documented to have a limited therapeutic efficacy showed marginal recovery of this population.

Our studies indicate that 2-IM profiling of lysosomes is a promising method for screening for potential lead compounds for Niemann–Pick diseases in an unbiased way, for potentially identifying suitable patient cohorts for clinical trials, for monitoring therapeutic efficacy, or for tracking disease progression. Although we currently cannot ascribe specific functions to the high-chloride, high-acidity population, the ability to resolve lysosome chemotypes in live cells may allow one to more quantitatively investigate the contribution of diverse lysosomal functions in health and disease.

Online content

Any methods, additional references, Nature Research reporting summaries, source data, statements of data availability and associated accession codes are available at https://doi.org/10.1038/s41565-018-0318-5.

Received: 1 May 2018; Accepted: 25 October 2018;
Published online: 3 December 2018

References

1. Settembre, C., Fraldi, A., Medina, D. L. & Ballabio, A. Signals from the lysosome: a control centre for cellular clearance and energy metabolism. *Nat. Rev. Mol. Cell Biol.* **14**, 283–296 (2013).
2. Fraldi, A., Klein, A. D., Medina, D. L. & Settembre, C. Brain disorders due to lysosomal dysfunction. *Annu. Rev. Neurosci.* **39**, 277–295 (2016).
3. Pu, J., Guardia, C. M., Keren-Kaplan, T. & Bonifacino, J. S. Mechanisms and functions of lysosome positioning. *J. Cell Sci.* **129**, 4329–4339 (2016).
4. Wasmeier, C., Hume, A. N., Bolasco, G. & Seabra, M. C. Melanosomes at a glance. *J. Cell Sci.* **121**, 3995–3999 (2008).
5. Faurschou, M. & Borregaard, N. Neutrophil granules and secretory vesicles in inflammation. *Microbes Infect.* **5**, 1317–1327 (2003).
6. Blott, E. J. & Griffiths, G. M. Secretory lysosomes. *Nat. Rev. Mol. Cell Biol.* **3**, 122–131 (2002).
7. Mizushima, N., Yoshimori, T. & Levine, B. Methods in mammalian autophagy research. *Cell* **140**, 313–326 (2010).
8. Pertoft, H., Wärmegård, B. & Höök, M. Heterogeneity of lysosomes originating from rat liver parenchymal cells. Metabolic relationship of subpopulations separated by density-gradient centrifugation. *Biochem. J.* **174**, 309–317 (1978).
9. Li, X. et al. A molecular mechanism to regulate lysosome motility for lysosome positioning and tubulation. *Nat. Cell Biol.* **18**, 404–417 (2016).
10. Matteoni, R. & Kreis, T. E. Translocation and clustering of endosomes and lysosomes depends on microtubules. *J. Cell Biol.* **105**, 1253–1265 (1987).
11. Pu, J. et al. BORC, a multisubunit complex that regulates lysosome positioning. *Dev. Cell* **33**, 176–188 (2015).
12. Kornak, U. et al. Loss of the ClC-7 chloride channel leads to osteopetrosis in mice and man. *Cell* **104**, 205–215 (2001).
13. Ba, Q., Raghavan, G., Kiselyov, K. & Yang, G. Whole-cell scale dynamic organization of lysosomes revealed by spatial statistical analysis. *Cell Rep.* **23**, 3591–3606 (2018).
14. Seiji, M., Shimao, K., Birbeck, M. S. C. & Fitzpatrick, T. B. Subcellular localization of melanin biosynthests. *Ann. NY Acad. Sci.* **100**, 497–533 (2006).
15. Raposo, G., Tenza, D., Murphy, D. M., Berson, J. F. & Marks, M. S. Distinct protein sorting and localization to premelanosomes, melanosomes, and lysosomes in pigmented melanocytic cells. *J. Cell Biol.* **152**, 809–824 (2001).
16. Chakraborty, K., Leung, K. & Krishnan, Y. High lumenal chloride in the lysosome is critical for lysosome function. *eLife* **6**, e28862 (2017).
17. Saha, S., Prakash, V., Halder, S., Chakraborty, K. & Krishnan, Y. A pH-independent DNA nanodevice for quantifying chloride transport in organelles of living cells. *Nat. Nanotech.* **10**, 645–651 (2015).
18. Van Dyke, R. W. Proton pump-generated electrochemical gradients in rat liver multivesicular bodies. Quantitation and effects of chloride. *J. Biol. Chem.* **263**, 2603–2611 (1988).
19. Luzio, J. P., Pryor, P. R. & Bright, N. A. Lysosomes: fusion and function. *Nat. Rev. Mol. Cell Biol.* **8**, 622–632 (2007).
20. Weinert, S. et al. Lysosomal pathology and osteopetrosis upon loss of H^+-driven lysosomal Cl^- accumulation. *Science* **328**, 1401–1403 (2010).
21. Guzman, R. E., Grieschat, M., Fahlke, C. & Alekov, A. K. ClC-3 is an intracellular chloride/proton exchanger with large voltage-dependent nonlinear capacitance. *ACS Chem. Neurosci.* **4**, 994–1003 (2013).
22. Biwersi, J., Tulk, B. & Verkman, A. S. Long-wavelength chloride-sensitive fluorescent indicators. *Anal. Biochem.* **219**, 139–143 (1994).
23. Arosio, D. et al. Simultaneous intracellular chloride and pH measurements using a GFP-based sensor. *Nat. Methods* **7**, 516–518 (2010).
24. Kuner, T. & Augustine, G. J. A genetically encoded ratiometric indicator for chloride. *Neuron* **27**, 447–459 (2000).
25. Surana, S., Shenoy, A. R. & Krishnan, Y. Designing DNA nanodevices for compatibility with the immune system of higher organisms. *Nat. Nanotech.* **10**, 741–747 (2015).
26. Modi, S., Nizak, C., Surana, S., Halder, S. & Krishnan, Y. Two DNA nanomachines map pH changes along intersecting endocytic pathways inside the same cell. *Nat. Nanotech.* **8**, 459–467 (2013).
27. Chu, T. C. et al. Aptamer:toxin conjugates that specifically target prostate tumor cells. *Cancer Res.* **66**, 5989–5992 (2006).
28. Pinheiro, A. V., Han, D., Shih, W. M. & Yan, H. Challenges and opportunities for structural DNA nanotechnology. *Nat. Nanotech.* **6**, 763–772 (2011).
29. Bhatia, D. et al. Quantum dot-loaded monofunctionalized DNA icosahedra for single-particle tracking of endocytic pathways. *Nat. Nanotech.* **11**, 1112–1119 (2016).
30. Prakash, V., Saha, S., Chakraborty, K. & Krishnan, Y. Rational design of a quantitative, pH-insensitive, nucleic acid based fluorescent chloride reporter. *Chem. Sci.* **7**, 1946–1953 (2016).
31. Modi, S., Halder, S., Nizak, C. & Krishnan, Y. Recombinant antibody mediated delivery of organelle-specific DNA pH sensors along endocytic pathways. *Nanoscale* **6**, 1144–1152 (2014).
32. Modi, S. et al. A DNA nanomachine that maps spatial and temporal pH changes inside living cells. *Nat. Nanotech.* **4**, 325–330 (2009).
33. Surana, S., Bhat, J. M., Koushika, S. P. & Krishnan, Y. An autonomous DNA nanomachine maps spatiotemporal pH changes in a multicellular living organism. *Nat. Commun.* **2**, 340 (2011).
34. Halder, S. & Krishnan, Y. Design of ultrasensitive DNA-based fluorescent pH sensitive nanodevices. *Nanoscale* **7**, 10008–10012 (2015).
35. Gough, P. J. & Gordon, S. The role of scavenger receptors in the innate immune system. *Microbes Infect.* **2**, 305–311 (2000).
36. Bhatia, D., Surana, S., Chakraborty, S., Koushika, S. P. & Krishnan, Y. A synthetic icosahedral DNA-based host–cargo complex for functional in vivo imaging. *Nat. Commun.* **2**, 339 (2011).
37. Chakraborty, K., Veetil, A. T., Jaffrey, S. R. & Krishnan, Y. Nucleic acid-based nanodevices in biological imaging. *Annu. Rev. Biochem.* **85**, 349–373 (2016).
38. Veetil, A. T. et al. Cell-targetable DNA nanocapsules for spatiotemporal release of caged bioactive small molecules. *Nat. Nanotech.* **12**, 1183–1189 (2017).
39. Surana, S., Bhatia, D. & Krishnan, Y. A method to study in vivo stability of DNA nanostructures. *Methods* **64**, 94–100 (2013).
40. Schuchman, E. H. & Desnick, R. J. Types A and B Niemann–Pick disease. *Mol. Genet. Metab.* **120**, 27–33 (2017).
41. Vanier, M. T. & Millat, G. Niemann–Pick disease type C. *Clin. Genet.* **64**, 269–281 (2003).
42. Desnick, R. J. & Schuchman, E. H. Enzyme replacement and enhancement therapies: lessons from lysosomal disorders. *Nat. Rev. Genet.* **3**, 954–966 (2002).
43. Ory, D. S. et al. Intrathecal 2-hydroxypropyl-β-cyclodextrin decreases neurological disease progression in Niemann-Pick disease, type C1: a non-randomised, open-label, phase 1–2 trial. *Lancet* **390**, 1758–1768 (2017).
44. Johnson, D. E., Ostrowski, P., Jaumouillé, V. & Grinstein, S. The position of lysosomes within the cell determines their luminal pH. *J. Cell Biol.* **212**, 677–692 (2016).
45. Kornhuber, J. et al. Identification of new functional inhibitors of acid sphingomyelinase using a structure–property–activity relation model. *J. Med. Chem.* **51**, 219–237 (2008).
46. Cenedella, R. J. Cholesterol synthesis inhibitor U18666A and the role of sterol metabolism and trafficking in numerous pathophysiological processes. *Lipids* **44**, 477–487 (2009).

47. He, X. et al. Characterization of human acid sphingomyelinase purified from the media of overexpressing Chinese hamster ovary cells. *Biochim. Biophys. Acta Protein Struct. Mol. Enzymol.* **1432**, 251–264 (1999).
48. Devany, J., Chakraborty, K. & Krishnan, Y. Subcellular nanorheology reveals lysosomal viscosity as a reporter for lysosomal storage diseases. *Nano Lett.* **18**, 1351–1359 (2018).
49. Aue, W. P., Bartholdi, E. & Ernst, R. R. Two-dimensional spectroscopy. Application to nuclear magnetic resonance. *J. Chem. Phys.* **64**, 2229–2246 (1976).

Acknowledgements

This work was supported by the University of Chicago Women's Board, Pilot and Feasibility award from an NIDDK center grant P30DK42086 to the University of Chicago Digestive Diseases Research Core Center, MRSEC grant no. DMR-1420709, Chicago Biomedical Consortium with support from the Searle Funds at The Chicago Community Trust, C-084, ANL-UChicago collaborative grant and University of Chicago start-up funds to Y.K. Y.K. is a Brain Research Foundation Fellow.

Author contributions

K.L., K.C., A.S. and Y.K. designed the project. K.L., K.C. and A.S. performed experiments. K.L., K.C., A.S. and Y.K. analysed the data. K.L., K.C., A.S. and Y.K. wrote the paper. All authors discussed the results and gave input on the manuscript.

Competing interests

The authors declare no competing interests.

Additional information

Supplementary information is available for this paper at https://doi.org/10.1038/s41565-018-0318-5.

Reprints and permissions information is available at www.nature.com/reprints.

Correspondence and requests for materials should be addressed to Y.K.

Publisher's note: Springer Nature remains neutral with regard to jurisdictional claims in published maps and institutional affiliations.

Methods

Reagents. All oligonucleotides used in this study were purified by high-performance liquid chromatography (HPLC) and obtained from IDT (Coralville, IA, USA) and IBA Lifesciences (Germany). The peptide nucleic acids oligomer was synthesized through standard solid-phase Fmoc chemistry on Nova Syn TGA resin (Novabiochem, Germany) using analytical grade reagents (Applied Biosystems, USA), purified by reverse-phase HPLC (Shimadzu, Japan) as previously reported[30] and stored at −20 °C until further use. Calcium nitrate tetrahydrate, sodium nitrate, sodium phosphate dibasic, sodium phosphate monobasic, magnesium sulfate anhydrous, glycerol, bovine serum albumin (66 kDa), nigericin, monensin, tributyltin chloride (TBT-Cl) and amitriptyline hydrochloride were obtained from Sigma (USA). Sodium chloride was purchased from Alfa Aesar (Haverhill, USA). Magnesium nitrate hexahydrate, sodium acetate anhydrous, sodium bicarbonate was purchased from Fisher Scientific (Hampton, USA). βCD and U18666A were purchased from Cayman Chemical (USA). CellLight Reagents BacMam 2.0, DMEM and FBS were purchased from molecular probes from Life Technologies (USA). Maleylated BSA (mBSA) was synthesized according to a previously published protocol[32]. Recombinant human SMPD1 protein was purchased from Novus Biologicals (USA). All other reagents were purchased from Sigma-Aldrich (USA) unless otherwise specified.

Sample preparation. 10 μM of relevant complementary oligonucleotides (Supplementary Table 1) were mixed in 10 mM sodium phosphate buffer and prepared as described previously[17,32].

Gel electrophoresis. Native polyacrylamide gels containing 12% acrylamide [19:1 acrylamide/bisacrylamide] were used for gel electrophoresis[17]. Gels were run in 1 × TBE buffer (100 mM Tris·HCl, 89 mM boric acid, and 2 mM EDTA, pH 8.3) at 4 °C. Gels were observed under a Biorad Universal Hood II Gel Doc System (Bio-Rad Laboratories, Inc.) using Image Lab Software 6.0.0 for image acquisition for Alexa 647 and Alexa 546 channels. After measurement, gels were stained with ethidium bromide (1 μg ml^{-1}) and observed.

In vitro fluorescence measurements. Fluorescence spectra were recorded by a FluoroMax-4 Scanning Spectrofluorometer (Horiba Scientific, USA) utilizing previously established protocols[32]. 200 nM of our reported pH sensor I^{mLY}[16], ChloropHore or ChloropHore$_{Ly}$ in UB4 buffer (20 mM HEPES, MES and sodium acetate, 150 mM KNO_3, 5 mM $NaNO_3$, 1 mM $Ca(NO_3)_2$ and $Mg(NO_3)_2$) of indicated pH were mixed and incubated at 37 °C for 30 min after which measurements were performed at 25 °C.

Determination of Stern–Volmer quenching constant, K_{sv}. K_{sv} was obtained from the slope of the in vitro Cl^- calibration curve where R/G was plotted against [Cl^-]. The denominator in the R/G is chloride sensitive whereas the numerator remains constant at different chloride concentration. Therefore, the R/G versus [Cl^-] plot is equivalent to the F_0/F versus [Cl^-] plot or the Stern–Volmer plot where F_0 is the intensity of BAC in 5 mM Cl^- and F is the intensity of BAC in various concentrations of Cl^-[50].

Circular dichroism spectroscopy. Circular dichroism spectroscopy scans were carried out on a Jasco J-1500 CD Spectrometer equipped with a temperature controller. 7 μM of unlabelled ChloropHore at pH 4.0 and 7.5 were prepared in 80 mM potassium phosphate buffer. Samples were then measured and represented as an average of three scans.

Cell culture methods and maintenance. BHK-21 cells, human dermal fibroblasts (HDF), J774A.1 and T47D cells were a kind gift from M. Gack (Department of Microbiology, the University of Chicago), J. Rowley's lab (University of Chicago), D. Nelson (Department of Pharmacological and Physiological Sciences, the University of Chicago) and G. Greene (The Ben May Department for Cancer Research, the University of Chicago), respectively. These cells were cultured in DMEM-F12 with 10% FBS, 100 U ml^{-1} penicillin and 100 μg ml^{-1} streptomycin and maintained at 37 °C under 5% CO_2. Fibroblasts AG01518, GM08429, GM00112, GM16195, GM13205, GM03252, GM03393, GM11097, GM18414, GM23162 and GM17910 were purchased from Coriell Institute (Camden, NJ) and cultured with the suggested protocols from Coriell Institute.

Competition experiments. HDF cells were washed with 1 × PBS buffer and then incubated with 10 μM of mBSA or BSA for 15 min. Next, cells were pulsed with 1 μM ChloropHore and 10 μM of mBSA or BSA in cell culture media for 1 h. Cells were washed with 1 × PBS three times and then imaged. Whole-cell intensities of 20 cells per dish in the A647 channel were quantified.

Colocalization experiments. Cells were transfected with LAMP1–RFP by CellLight Reagents BacMam 2.0 according to the manufacturer's protocol. Briefly, CellLight Reagents were added to the cells at approximately 20 particles per cell and incubated for 10 h. Transfected cells were then pulsed with 0.25 mg ml^{-1} of 10 kDa FITC–Dextran (FITC-Dex) for 1 h, chased for 16 h and was followed by imaging. Crosstalk and bleed-through were measured and found to be negligible between the RFP channel and the FITC–Dex channel. These experiments revealed that the pulse-chase time point selected for FITC–Dex labelling of lysosomes showed approximately 80% colocalization with LAMP1–RFP.

We utilized lysosomes pre-labelled with TMR–Dex to examine the trafficking timescales for our ChloropHore. Pre-labelled cells were pulsed with 1 μM of ChloropHore and chased for indicated time and imaged. Crosstalk and bleed-through were recorded and discovered to be negligible between the TMR channel and A647 channel. Pearson's correlation coefficient (PCC) measures the pixel-by-pixel covariance of two images while it ranges from 0–1, and 1 indicates complete colocalization. PCCs are examined by the tool in ImageJ/Fiji 2.0.0-rc-54/1.51 h. On pixel shift, PCC values decrease significantly suggesting non-random colocalization.

In cellulo clamping. pH and chloride clamping were carried out with ChloropHore using a previously published protocol from our lab[16,17,26,32,33]. HDF cells were pulsed for 1 h and chased for 2 h with 2 μM of Chlorophore. After labelling, cells were fixed by 200 ml 4% paraformaldehyde for 5 min at 25 °C. The fixed cells were washed with 1 × PBS three times and incubated in the chloride clamping buffer of indicated pH and chloride concentration that also contained 50 μM nigericin, 50 μM monensin and 25 μM tributyltin chloride (TBT-Cl) for 1 h at 25 °C. Clamping buffers with various concentration of chloride ions were prepared by adding chloride positive buffer (150 mM KCl, 5 mM NaCl, 1 mM $CaCl_2$, 1 mM $MgCl_2$, 10 mM HEPES, MES, sodium acetate) to a chloride negative buffer (150 mM KNO_3, 20 mM $NaNO_3$, 1 mM $Ca(NO_3)_2$, 1 mM $Mg(NO_3)_2$, 10 mM HEPES, MES, sodium acetate) at the same indicated pH in different ratios[17]. The cells were then imaged in clamping buffer.

Single-lysosome clamping. After first round cell clamping and imaging, the first round clamping buffer was replaced with the second round clamping buffer, which contained 50 μM nigericin, 50 μM monensin and 25 μM TBT-Cl with either a pH or [Cl^-] difference from the first round clamping buffer. The cells were incubated in the second clamping buffer for 1 h at room temperature before they were imaged.

DNA stability assay. A DNA stability assay was performed as described previously[39]. Cells were pulsed with 1 mg ml^{-1} TMR–Dex for 1 h and chased for 16 h. The TMR–Dex-labelled cells were pulsed with 2 μM of ChloropHore for 1 h, and chased for indicated time points for imaging.

Lysosomal pH and chloride measurements. Fibroblast cells were pulsed with 2 μM of our reported pH sensor I^{mLY}, ChloropHore or ChloropHore$_{Ly}$ for 1 h, chased for 9 h (30 min pulse and 1 h chase for J774.A1, BHK-21 and T47D cells) and then washed with 1 × PBS and imaged.

2-IM on addition of lysosomal proton pump and ion channel blocker. On lysosome labelling, a final concentration of 500 nM bafilomycinA1 and 300 μM of 5-nitro-2-(3-phenylpropylamino) benzoic acid (NPPB) were added to cells and incubated for 45 min. Cells were then washed with PBS and imaged in Hank's Balanced Salt Solution (HBSS) containing the respective blocker compounds.

Preparation of pharmacologically induced cell culture model for Niemann–Pick type A/B (NP-A/B) and type C (NP-C). Niemann–Pick type A/B and C models were prepared according to the previously reported method[16]. Cells were incubated with 65 μM of the ASM inhibitor amitriptyline (AH) and 20 μM of the NPC1 inhibitor U18666A[46] for 24 h to create the NP-A/B and NP-C models, respectively[45]. The cells were pulsed with 2 μM of ChloropHore$_{Ly}$ and either 65 μM AH or 20 μM U18666A for 1 h, chased with either 65 μM AH or 20 μM U18666A for 9 h and then washed with 1 × PBS and imaged.

Lysosomal population rescue using ASM and βCD. Recombinant human ASM was incubated with NP-A/B patient cells according to the previous method[47]. Primary human fibroblasts derived from NP-A/B patients were maintained in DMEM medium with 1% FBS for 24 h. The medium was then changed to DMEM with 1% FBS containing 0.2% BSA and 5 μg of ASM. After 24 h, the cells were pulsed with 2 μM of ChloropHore$_{Ly}$ for 1 h, chased for 9 h and then washed with 1 × PBS and imaged. Primary human fibroblasts from NP-C patients were incubated with 50 μM *o*-hydroxypropyl-β-cyclodextrin (βCD) for 24 h. The cells were pulsed with 2 μM of ChloropHore$_{Ly}$ and 50 μM βCD for 1 h, chased with 50 μM of βCD for 9 h and then washed with 1 × PBS and imaged.

Microscopy. Imaging was conducted on a wide field IX83 inverted microscope (Olympus, USA) with 60×, 1.42 NA, phase contrast oil immersion objective (PLAPON, USA) and Evolve Delta 512 EMCCD camera (Photometrics, USA). Filter wheel, shutter and CCD camera were controlled by Metamorph Premier Version 7.8.12.0 (Molecular Devices, LLC, USA). Images were acquired using previously established protocols[16].

Image analysis. Images were analysed with ImageJ/Fiji 2.0.0-rc-54/1.51 h. pH and chloride measurements were performed as described previously[16,17,32].To generate a density plot to represent lysosomal populations we first plotted the individual D/A

(*y* axis) versus the corresponding R/G (*x* axis) values for each lysosome that were obtained for a given fibroblast sample comprising ~60 cells and ~600 lysosomes. Density plots were generated using 2D Kernel Density plot on Origin 2018 SR1 b9.5.1.195 (OriginLab, USA). This converted the individual scatter points into a population matrix as a probability density function. The density plot was then pseudo-coloured to represent high density in red (values close to 1) and low density in blue (values closer to 0). We discarded those points with <10% probability on the plot. For normalization between days, we designated the point of highest density (value = 1) of normal HDF cells as the centre of the plot with *x*,*y* coordinates (1,1). To normalize between experiments done on different days we always measured the lysosomal pH and Cl^- of a sample of normal HDF cells as well, the density plot of which served as the reference. All density plots acquired on the same day with the same settings were thus normalized to the HDF cell density plots to enable comparison of data across different days.

Data were normalized as follows. The maximum and minimum values of D/A and R/G of the reference HDF cell density plot were considered as reference points to *x* and *y* align the lysosome profile of a given sample. These maxima and minima were considered as 25% and 75% of the density plot, respectively. The maxima and minima of D/A and R/G of newly obtained HDF cell datasets were adjusted to this accordingly, such that they overlaid. The centre of the density profile (the point displaying highest density) was then adjusted to $x = 1$, $y = 1$ coordinates. The density plot from other samples in the same set of experiments was aligned using the identical parameters used to align the HDF cell dataset with the reference HDF cell dataset. The density plots of HDF cells obtained from independent experiments performed on different days were normalized and are shown in Supplementary Fig. 6 to demonstrate the reproducibility of this method.

Reporting Summary. Further information on research design is available in the Nature Research Reporting Summary linked to this article.

Data availability

The data that support the plots within this paper and the findings of this study are available from the corresponding author upon reasonable request.

References

50. Boaz, H. & Rollefson, G. K. The quenching of fluorescence. Deviations from the Stern–Volmer law. *J. Am. Chem. Soc.* **72**, 3435–3443 (1950).

nature research

Corresponding author(s): Yamuna Krishnan

Reporting Summary

Nature Research wishes to improve the reproducibility of the work that we publish. This form provides structure for consistency and transparency in reporting. For further information on Nature Research policies, see Authors & Referees and the Editorial Policy Checklist.

Statistical parameters

When statistical analyses are reported, confirm that the following items are present in the relevant location (e.g. figure legend, table legend, main text, or Methods section).

n/a	Confirmed	
☐	☒	The exact sample size (*n*) for each experimental group/condition, given as a discrete number and unit of measurement
☐	☒	An indication of whether measurements were taken from distinct samples or whether the same sample was measured repeatedly
☒	☐	The statistical test(s) used AND whether they are one- or two-sided *Only common tests should be described solely by name; describe more complex techniques in the Methods section.*
☒	☐	A description of all covariates tested
☐	☒	A description of any assumptions or corrections, such as tests of normality and adjustment for multiple comparisons
☐	☒	A full description of the statistics including central tendency (e.g. means) or other basic estimates (e.g. regression coefficient) AND variation (e.g. standard deviation) or associated estimates of uncertainty (e.g. confidence intervals)
☒	☐	For null hypothesis testing, the test statistic (e.g. *F*, *t*, *r*) with confidence intervals, effect sizes, degrees of freedom and *P* value noted *Give P values as exact values whenever suitable.*
☒	☐	For Bayesian analysis, information on the choice of priors and Markov chain Monte Carlo settings
☒	☐	For hierarchical and complex designs, identification of the appropriate level for tests and full reporting of outcomes
☐	☒	Estimates of effect sizes (e.g. Cohen's *d*, Pearson's *r*), indicating how they were calculated
☐	☒	Clearly defined error bars *State explicitly what error bars represent (e.g. SD, SE, CI)*

Our web collection on statistics for biologists may be useful.

Software and code

Policy information about availability of computer code

Data collection	Metamorph Premier ver 7.8.12.0 (Molecular Devices, LLC, USA) for image acquisition, FluorEssence ver 6.5 for fluorescence measurements, Image Lab™ Software 6.0.0 for PAGE image acquisition
Data analysis	Origin 2018 SR1 b9.5.1.195 (OriginLab Corporation, Northampton, MA, USA) for data plotting, ImageJ/Fiji 2.0.0-rc-54/1.51h for image analysis

For manuscripts utilizing custom algorithms or software that are central to the research but not yet described in published literature, software must be made available to editors/reviewers upon request. We strongly encourage code deposition in a community repository (e.g. GitHub). See the Nature Research guidelines for submitting code & software for further information.

Data

Policy information about availability of data

All manuscripts must include a data availability statement. This statement should provide the following information, where applicable:

- Accession codes, unique identifiers, or web links for publicly available datasets
- A list of figures that have associated raw data
- A description of any restrictions on data availability

The raw data that supports all the figures in this paper and other findings of this study are available from the corresponding author upon reasonable request.

Field-specific reporting

Please select the best fit for your research. If you are not sure, read the appropriate sections before making your selection.

☒ Life sciences ☐ Behavioural & social sciences ☐ Ecological, evolutionary & environmental sciences

For a reference copy of the document with all sections, see nature.com/authors/policies/ReportingSummary-flat.pdf

Life sciences study design

All studies must disclose on these points even when the disclosure is negative.

Sample size	Sample size was not predetermined. Two ions measurement (2-IM) experiment were repeated two times independently. Other experiments described in this manuscript were performed three times independently. These sample sizes are widely adopted in the field of chemical biology.
Data exclusions	No data were excluded from the analyses.
Replication	In vitro fluorescence assays, steady state and kinetic fluorescence imaging were all performed independently in at least triplicates while 2 ions measurement (2-IM) imaging was performed in duplicate to ensure reproducibility. All replications were successful.
Randomization	Allocation was random. Cultured dishes containing various types of cells were randomized for selection in imaging experiments and biochemical assays.
Blinding	We used DNA based quantitative imaging technology to compare chloride ions and pH levels under different cellular conditions. Thus, it was not necessary to design a blinding group allocation.

Reporting for specific materials, systems and methods

Materials & experimental systems

n/a	Involved in the study
☐	☒ Unique biological materials
☒	☐ Antibodies
☐	☒ Eukaryotic cell lines
☒	☐ Palaeontology
☒	☐ Animals and other organisms
☐	☒ Human research participants

Methods

n/a	Involved in the study
☒	☐ ChIP-seq
☒	☐ Flow cytometry
☒	☐ MRI-based neuroimaging

Unique biological materials

Policy information about availability of materials

Obtaining unique materials	All unique biological materials are readily available from the authors or from IDT/IBALifesciences

Eukaryotic cell lines

Policy information about cell lines

Cell line source(s)	Mouse alveolar macrophage J774A.1 cells were a kind gift from Prof Deborah Nelson (Department of Pharmacological and Physiological Sciences, the University of Chicago) T47D cells were a kind gift from Prof. Geoffrey Greene (The Ben May Department for cancer research, the University of Chicago,). BHK-21 cells were a kind gift from Prof. Michaela Gack (Department of microbiology, the University of Chicago,).
Authentication	No further authentication was performed after receiving the cells as a gift.
Mycoplasma contamination	We routinely check our cell lines for Mycoplasma contamination using Hoechst staining and all cell lines used in this study turned out to be negative for Mycoplasma contamination.

Commonly misidentified lines (See ICLAC register)	No commonly misidentified cell lines were used.

Human research participants

Policy information about studies involving human research participants

Population characteristics	Primary Human dermal fibroblasts (HDF) were a kind gift from Late Professor Janet Rowley's Lab at the University of Chicago. Primary fibroblasts GM08429, AG01518, GM00112, GM16195, GM13205, GM03252, GM11097, GM18414, GM23162 and GM17910 were purchased from a reliable public repository i.e., Coriell Institute (Camden, NJ)
Recruitment	Three patient samples corresponding to NP-A and NP-C disease and two for NP-B were studied based on sample availability, common mutations and characterization by enzyme activity